

Three-dimensional modelling of underwater noise produced by a bulk carrier vessel and estimation of its environmental impact^{a)}

Pavel S. Petrov,^{1,b)}  Andrey G. Tyshchenko,¹ and Alexander O. MacGillivray² 

¹*Geophysical Fluid Dynamics Laboratory, Il'ichev Pacific Oceanological Institute, Vladivostok, 690041, Russia*

²*JASCO Applied Sciences, Victoria, British Columbia, Canada*

ABSTRACT:

This study presents the results of three-dimensional (3D) propagation modeling of noise from a transiting bulk carrier vessel. In the simulated scenario, the surface vessel is moving past a bottom-mounted hydrophone system. Sound levels are estimated in decidecade frequency bands as the vessel transits past the hydrophone, and the simulation results are compared against real measured data. The modelling is performed using the program AMPLE, which is based on the wide-angle mode parabolic equation theory for simulating 3D broadband acoustic fields in a shallow sea. The model is used to investigate the effect of 3D phenomena on the surface vessel sound propagation. It is shown that an inaccuracy of the noise simulation associated with the use of a two-dimensional model can be as high as 7–10 dB for certain distances and for frequency bands over which a major part of the source energy is distributed. An approach to the selection of data-adjusted media parameters based on the Bayesian optimization is suggested, and the influence of the various parameters on the sound levels is discussed. © 2024 Author(s). All article content, except where otherwise noted, is licensed under a Creative Commons Attribution (CC BY) license (<https://creativecommons.org/licenses/by/4.0/>). <https://doi.org/10.1121/10.0026238>

(Received 28 February 2024; revised 27 April 2024; accepted 21 May 2024; published online 7 June 2024)

[Editor: Christ de Jong]

Pages: 3702–3714

I. INTRODUCTION

Currently efficient and adequate mapping of shipping noise and estimation of its impact on the environment constitutes one of the main challenges in underwater acoustics (Ainslie *et al.*, 2021b; Jiang *et al.*, 2020; MacGillivray and de Jong, 2021; Merchant *et al.*, 2012; Simard *et al.*, 2016; Wales and Heitmeyer, 2002). It is widely accepted that shipping is one of the main anthropic sources of noise that affects marine ecosystems, especially in coastal areas near major ports. Systematic exposure to high levels of sound may have a negative impact on the populations of various species of marine mammals, fish, and even invertebrates, and exact quantification of acceptable threshold currently attracts significant research effort (Erbe *et al.*, 2019; Southall *et al.*, 2019; Southall *et al.*, 2017). On the other hand, shipping noise can be a valuable source of information about the medium. For example, in Gervaise *et al.* (2012) and Simard *et al.* (2016) the ship noise is used as a source of opportunity for performing geoacoustic inversion of bottom parameters. In Knobles (2015) both the ship source spectrum and seabed parameters were estimated using a statistical inference method under the assumption that a vessel can be represented as a point source, while Tollefsen *et al.* (2021) simultaneously estimated the ship source spectra and

seabed model parameters using a Bayesian inversion method and a multiple point-source model to represent merchant ships.

In addition to the direct measurements, the mapping of the distribution of the noise levels over large areas of a sea requires adequate tools for sound propagation modelling. In recent years, several classes of computational tools have been developed in the framework of different mathematical approaches including ray- and Gaussian-beam-based methods (de Moraes Calazan and Rodríguez, 2018; Oliveira *et al.*, 2021; Porter, 2019), three-dimensional (3D) parabolic equation theory (Lin *et al.*, 2013; Sturm, 2016), energy flux technique (Özkan Sertlek and Ainslie, 2014; Sertlek *et al.*, 2018) and mode parabolic equations (Petrov *et al.*, 2024; Petrov *et al.*, 2020) [i.e., vertical modes combined with two-dimensional (2D) parabolic equations for computing amplitudes of the modal expansion of the field]. Most of these methods underwent a thorough verification in various benchmark problems featuring some idealized environment models (see, e.g., Petrov *et al.*, 2020) and a monopole-type point source (in most cases a time-harmonic one). Despite aforementioned impressive advances in the development of numerical methods for the simulation of sound fields in underwater acoustics in the past two decades, when it comes to the needs of the industry and real-world applications, there are still many questions related to the efficiency and accuracy balance, as well as to correct reproduction of various noise sources in computational models.

^{a)}This paper is part of a special issue on Verification and Validation of Source and Propagation Models for Underwater Sound.

^{b)}Email: petrov@poi.dvo.ru

In order to address these questions several workshops on sound propagation modelling have been organized recently, including a 2022 Cambridge Joint Industry Programme Acoustic Modelling (JAM) workshop (Ainslie *et al.*, 2019; Ainslie *et al.*, 2023). One of the model validation problems offered by the organizers to the participants was concerned with simulation of the noise produced by a bulk carrier vessel. In this scenario, the vessel is moving past an underwater listening station (ULS) deployed close to Saturna Island near the Port of Vancouver (MacGillivray *et al.*, 2022) (see Fig. 1). The participants were provided with vessel track data [its transit of the closest point of approach (CPA) to the monitoring station], the effective source level of an equivalent monopole, and the information on the environment including bathymetry in the area, historical sound speed profiles (SSP) for three months, and some limited data on the geoacoustic parameters of the bottom layers. The goal was to simulate the distribution of the sound levels over decade bands (Ainslie *et al.*, 2021a; Ainslie *et al.*, 2022) for various distances between the vessel and the monitoring station. The measurement data taken by the monitoring station were made available to the participants *a posteriori* for the validation of the modelling results.

The goal of the present study is to present the results of our work on this scenario and to share our understanding regarding of the possible ways to improve the shipping noise modelling. The simulations in this study were carried out using the AMPLE code (Petrov and Tyshchenko, 2020; Tyshchenko *et al.*, 2021) based on the mode parabolic equations technique (Petrov *et al.*, 2020). This method features the capability to perform full-wave modelling of sound propagation in the 3D geoacoustic waveguide of a shallow sea. Thus, one of the key results of this work is an investigation of the role played by 3D effects in shipping noise propagation. Although the propagation distances in the considered scenario are somewhat shorter than is usually required for the 3D features of the sound field to develop, the strongly range-dependent environment in the narrow strait where the monitoring station was deployed favours the manifestation of the related effects.

In the course of our work on the workshop scenario, we discovered that it was impossible to achieve satisfactory agreement between the measurements and the simulation with the bottom parameters suggested by the organizers. To overcome this difficulty, we performed an optimization of the geoacoustic parameters aimed at achieving a better fit of

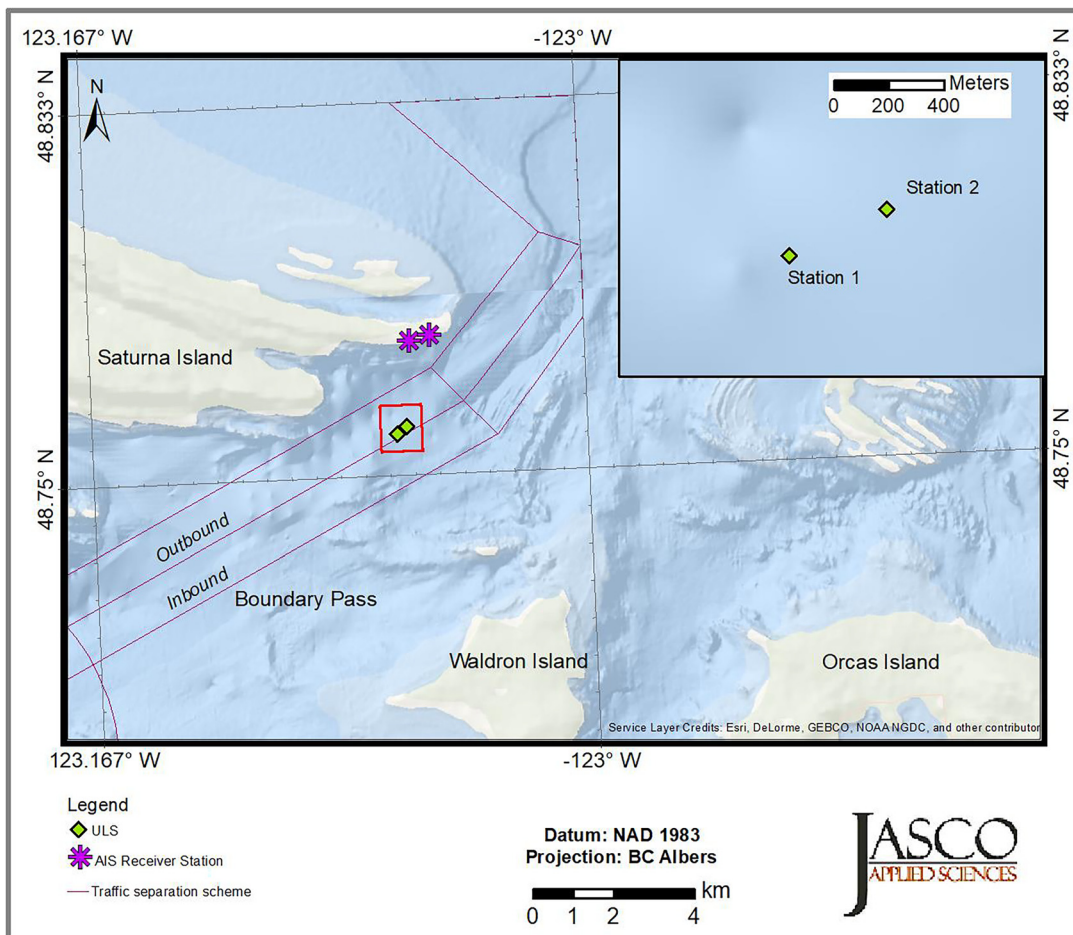


FIG. 1. (Color online) The measurements area and the noise monitoring stations, picture courtesy of Zizheng Li and Graham Warner (JASCO Applied Sciences).

the noise levels distribution at CPA, and afterward, the resulting measurement-adjusted bottom model was used for the modelling of noise for all positions of the vessel in the course of the CPA transit. We believe that such an optimization approach is practical when performing vessel noise monitoring in practice.

Another challenge for the noise field simulation was related to the fact that we had a single reception point (i.e., the monitoring station) while the position of the source was slowly moving. Clearly, full 3D broadband modelling of the field for every source position is not feasible even with the most efficient codes. For this reason, we had to use the reciprocity principle (Jensen *et al.*, 2011) and compute the 3D acoustic field for all frequencies involved as if the source was located at the monitoring station. In this case, the model can be run once to compute the noise levels along all points of the vessel track. This approach must be used with due care when strong currents are present in the area of interest, and the equations of sound propagation must be adjusted in order to take the moving media effects into account.

At the same time, we expect it to produce acceptable results whenever the current velocity projection onto the source-receiver line is sufficiently small.

The paper is organized as follows: Sec. II presents a brief scenario description. Section III briefly describes the AMPLE sound propagation modelling tool, and the modelling results are discussed in Sec. IV, where noise distributions are computed both for original and optimized media parameters. Key results, findings, and observations are summarized in Sec. V.

II. SCENARIO DESCRIPTION

As was mentioned in Sec. I, the JAM workshop scenario under consideration corresponds to the transit of a bulk carrier vessel past a hydrophone system deployed in a strait near Saturna Island close to the Port of Vancouver. The vessel transiting past the hydrophones of a measurement system was tracked via the Automated Identification System (AIS). Source level data provided to the workshop participants were generated by an automated system (JASCO PortListen) that computes vessel source levels within a data window defined by a $\pm 30^\circ$ azimuth angle centred from the CPA to the hydrophone. Source levels from a single transit of a vessel of opportunity were analyzed on the basis of SPL versus distance measurements in decidecade frequency bands with centre frequencies from 10 Hz to 250 kHz. PortListen computed propagation loss

from the hydrophone to the vessel CPA using a wave equation model, assuming a source depth equal to 70% of the vessel draft at the time of measurement. Additional details regarding the automated source level analysis performed by PortListen are provided by Hannay *et al.* (2016). For the workshop validation scenarios, model predictions were compared to mean square pressure versus frequency, $\overline{p_{ddec}^2}(f)$, and sound exposure versus frequency, $E_{p,ddec}(f)$, in decidecade bands, as measured on the ULS using a temporal observation window of 1 s at distances of up to 3.3 km from the hydrophone. Acoustic quantities are as defined in ISO 18405:2017 (ISO, 2017; Ainslie *et al.*, 2021a).

The bathymetry in the area of vessel transit is shown in Fig. 2 where we introduced a Cartesian coordinate system centered at the receiver location and with an x -axis aligned along the bulk carrier track. The bottom of the area consists of an upper sediment layer (which is formed by fine-grained sand) overlying a bedrock substrate (the values of the geoacoustic parameters of the bottom suggested by the workshop organizers are given in Table II).

The historical SSP for the Salish Sea available to the workshop participants are presented in Fig. 3 (note that the measurements took place in November, but the SSP data for October and December were also provided). The effective source spectrum of the bulk carrier is shown in Fig. 4. Note that it corresponds to the source level of an equivalent monopole (ISO, 2017) and no information on the source directivity was given in the problem statement.

The goal of the CPA transit simulation was to reproduce acoustic energy distribution over decidecade frequency bands $E_{p,ddec}(f)$ defined as

$$E_{p,ddec}(f_c, d) = 2 \int_{f_1}^{f_2} |P(f, d)|^2 df,$$

where f_c is the central frequency of the band $[f_1, f_2]$, $P(f, d)$ is the spectrum at the receiver computed for a time window of 1 s for a given point of the CPA transit, and d is the distance from the ship to the hydrophone of the measurement system. Another important quantity is $\overline{p_{ddec}^2}(f)$ at CPA computed by the formula

$$\overline{p_{ddec}^2}(f) = E_{p,ddec}(f_c, d_{CPA})/T,$$

where T is the temporal observation window (hereafter $T = 1$ s), and d_{CPA} is the distance from the ship to the measurement system at CPA.

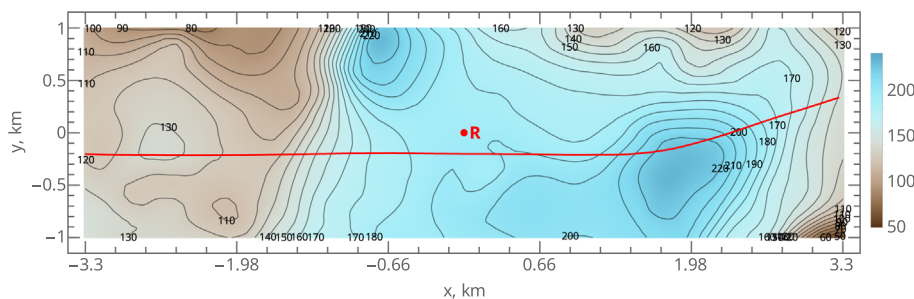


FIG. 2. (Color online) Bathymetry chart in the monitoring area and the vessel track in the Cartesian coordinates with the x -axis aligned approximately along the track and the receiver position specified by R.

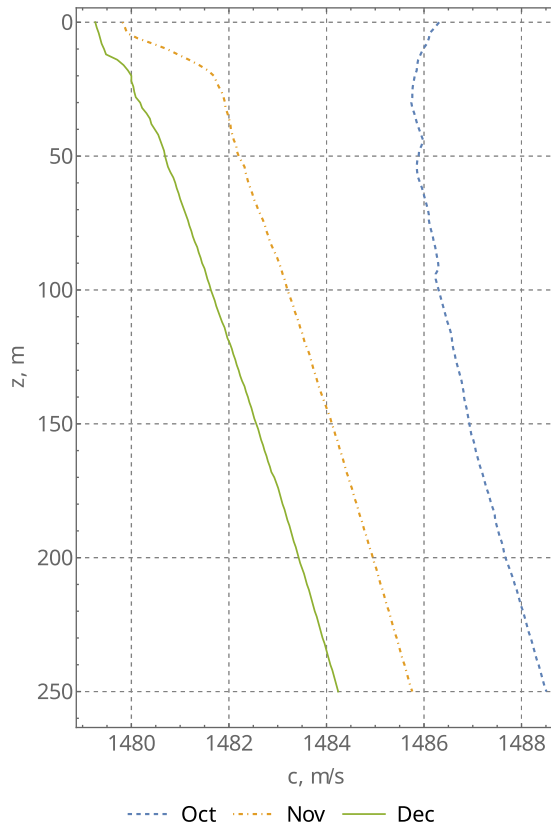


FIG. 3. (Color online) Historical data on SSPs in the area of interest.

As we use a normal-mode-based model AMPLE, we decided that our attention is restricted to the frequency band EC2 (8.91–891 Hz). It was requested that the modelling results are averaged over decidecade frequency bands.

III. COMPUTATIONAL MODEL AMPLE

This section is dedicated to a brief description of the AMPLE modelling program and the mathematical concepts involved. The program is implemented in C++ and

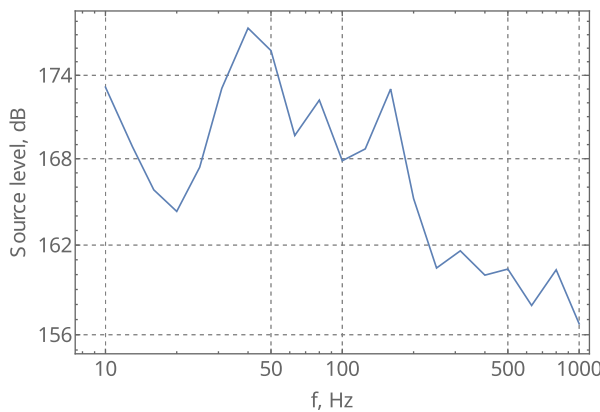


FIG. 4. (Color online) Decidecade band source level spectrum of the bulk carrier (re $1 \mu\text{Pa}^2 \text{m}^2$) as measured at the CPA to the underwater listening station. The assumed source depth was 6.2 m. The identity and particulars of the vessel were anonymized and not shared with workshop participants. The length of the vessel is approximately 185 m and the beam approximately 30 m.

available together with its source (Petrov and Tyshchenko). It performs broadband modelling of sound propagation in 3D shallow-water waveguides. The configuration files allow the user to specify bathymetry, SSP, and the structure of the bottom layers in the simulation area.

A. Mathematical foundations

It is known that the acoustic field $p(x, y, z)$ generated by a time-harmonic point source of frequency f satisfies the 3D Helmholtz equation,

$$\frac{\partial^2 p}{\partial x^2} + \frac{\partial^2 p}{\partial y^2} + \frac{\partial^2 p}{\partial z^2} + \frac{\omega^2}{c^2} (1 + i\eta\beta)^2 = -\delta(x)\delta(y)\delta(z - z_s), \quad (1)$$

where $\omega = 2\pi f$ is the angular frequency, $c = c(x, y, z)$ is the sound velocity, β is the attenuation coefficient, and $\eta = 1/40\pi \log_{10} e$. Furthermore, the acoustic pressure can be expressed as a truncated expansion over normal modes ϕ_j ,

$$p(x, y, z) = \sum_{j=1}^N A_j(x, y)\phi_j(z, x, y), \quad (2)$$

where $k_j = k_j(x, y)$ are their respective horizontal wavenumbers obtained by solving the Sturm-Liouville problem,

$$\begin{cases} \frac{d^2 \phi_j}{dz^2} + \frac{\omega^2}{c^2} \phi_j = k_j^2 \phi_j, \\ \phi_j|_{z=0} = 0, \quad \phi_j|_{z=H} = 0, \\ \phi_j|_{z=h-0} = \phi_j|_{z=h+0}, \quad \frac{1}{\rho} \frac{d\phi_j}{dz} \Big|_{z=h-0} = \frac{1}{\rho} \frac{d\phi_j}{dz} \Big|_{z=h+0}, \end{cases} \quad (3)$$

for a fixed pair of values (x, y) , i.e., in some vertical section of the computational area $z \in [0, H]$. Note that the second line of Eq. (3) consists of the pressure-release (zero-Dirichlet) boundary condition at the ocean surface and the lower boundary of the computational domain $z = H$, while the third line represents the continuity conditions at the water-bottom interface $z = h(x, y)$.

Under the adiabatic assumption (i.e., when the mode coupling is negligible), it can be shown that the mode amplitudes $A_j = A_j(x, y)$ in Eq. (2) satisfy the horizontal refraction equation,

$$\frac{\partial^2 A_j}{\partial x^2} + \frac{\partial^2 A_j}{\partial y^2} + k_j^2 A_j = -\phi(z_s)\delta(x)\delta(y). \quad (4)$$

Cancelling out the principal oscillation (using some reference horizontal wavenumber $k_{j,0}$),

$$A_j(x, y) = e^{ik_{j,0}x} B_j(x, y), \quad (5)$$

one can obtain the following one-way pseudo differential mode parabolic equation (PDMPE) for the envelope functions B_j ,

$$\frac{\partial B_j}{\partial x} = ik_{j,0} \left(\sqrt{1 + \hat{L}_j} - 1 \right) B_j, \quad (6)$$

where the differential operator \hat{L}_j satisfies $k_{j,0}^2 \hat{L}_j = \partial^2 / \partial y^2 + k_j^2 - k_{j,0}^2$.

PDMPE Eq. (6) can be approximately solved by a variety of techniques including, e.g., powerful pseudospectral methods and the split-step Padé approach (Collins, 1993; Petrov and Antoine, 2020). The latter one is used in the AMPLE program, and various numerical aspects of the PDMPE solution were developed in recent research (Petrov et al., 2020).

B. The program implementation and performance

The program AMPLE (Petrov and Tyshchenko, 2020) was developed at Il'ichev Pacific Oceanological Institute (POI) specifically for the purposes of broadband anthropic noise monitoring and simulation. It is written in C++ and utilizes a simple command-line interface with media and computation parameters being provided in a JSON (JavaScript Object Notation) configuration file. The program uses point-source model (as described in Sec. III A) and utilizes the simple ray starter for PDMPEs (Petrov et al., 2020). Modal functions and wavenumbers are computed using the CAMBALA (Petrov et al., 2020) utility. For this scenario we slightly adjusted AMPLE options across the frequency range (that was divided into 4 parts) in order to slightly reduce the total computational time (see Table I).

All computations were done on a regular rectangular grid $x \in [20, 3320], y \in [-1000, 1000]$ with the steps sizes $\Delta x = 1, \Delta y = 0.125$, for the computations in both positive and negative directions of x -axis from the source, $z_s = 192.7$. A perfectly matched layer was used to truncate the computational domain in y (see Petrov et al., 2020) for the details on the domain truncation). Acoustic modes we computed using the CAMBALA library that utilizes a finite-difference discretization of the Sturm-Liouville problem [Eq. (3)] (the actual computations were performed using the step size $\Delta z = 0.1$ in z).

Twenty CPU processes were utilized during computation. The acoustic fields were output on a smaller regular grid $n_x = 331, n_y = 321, n_z = 11$. $E_{p,ddec}(f)$ were then obtained using a Wolfram Mathematica script.

IV. MODELLING RESULTS

As mentioned in the introduction, we used a reciprocity principle to perform the vessel noise simulation. More

TABLE I. Media parameters used in the simulation for different frequency ranges.

Frequency range Hz			Substrate thickness m	Number of modes	Comp. time min
f_0	f_1	Δf			
8	24	1	1200	8	20
25	99	1	1200	28	220
100	298	2	800	80	530
300	892	4	600	160	1470

precisely, we set up the source at the depth of 192.7 m at $x = 0, y = 0$ (the actual location of the measurement system) and performed the computation of the sound pressure field for all frequencies from 8 Hz to 891 Hz in the area $-3.3 \text{ km} \leq x \leq 3.3 \text{ km}, 1 \text{ km} \leq y \leq 1 \text{ km}$ at $z = 6.2 \text{ m}$, which is specified in the scenario description as the effective depth of the source (see Cartesian coordinates in Fig. 2). In other words, it was more efficient to simulate the sound propagation from the receiver to the source (hereafter this is called reciprocal modelling) than vice versa (direct modelling). After computing the horizontal cross section of the acoustic field for a given frequency, acoustic pressure values were interpolated onto all points of the vessel track.

It was originally suggested by the organizers that the environment should be considered range-independent (i.e., homogeneous in x, y). Indeed, such simplification could be reasonable for distances of about 3 – 4 km for which horizontal refraction effects are usually insignificant. We decided, however, that it is interesting to evaluate the significance of these effects in this scenario. Thus, all computations were performed using a full 3D AMPLE code (in which the pseudodifferential parabolic equations were solved both in positive and negative directions of the x -axis) and its simple 2D counterpart (which is computationally cheaper by approximately a factor of 400).

The first modelling results we obtained were rather discouraging. Even at the CPA the levels of the simulated noise substantially exceeded those obtained from the measurements data (see Fig. 5). The difference is even more noticeable when comparing the noise levels for the CPA transit on a distance-frequency diagram as shown in Fig. 6. Although partly higher levels in the simulated field can be explained by the fact that AMPLE program does not take bottom elasticity into account (which typically results in higher transmission loss), the discrepancy is too large to be explained exclusively by this factor. Other possible explanations of this disagreement include an inaccuracy in the information on the geoacoustic parameters of the bottom, a disagreement

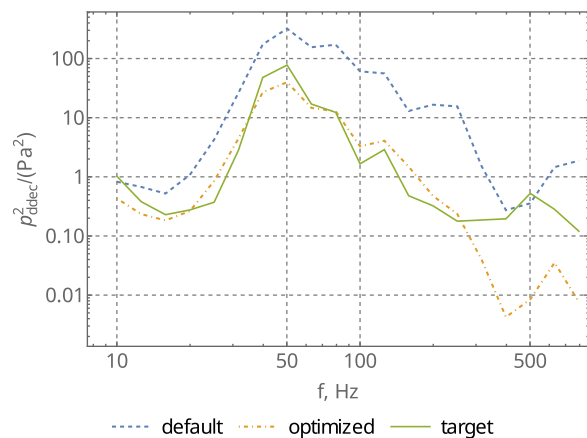


FIG. 5. (Color online) Noise distribution over frequencies at CPA of the vessel transit track obtained from measurements data (solid line), and from the modelling results using the default (dashed line) and the optimized (dashed-dotted line) values of environment parameters.

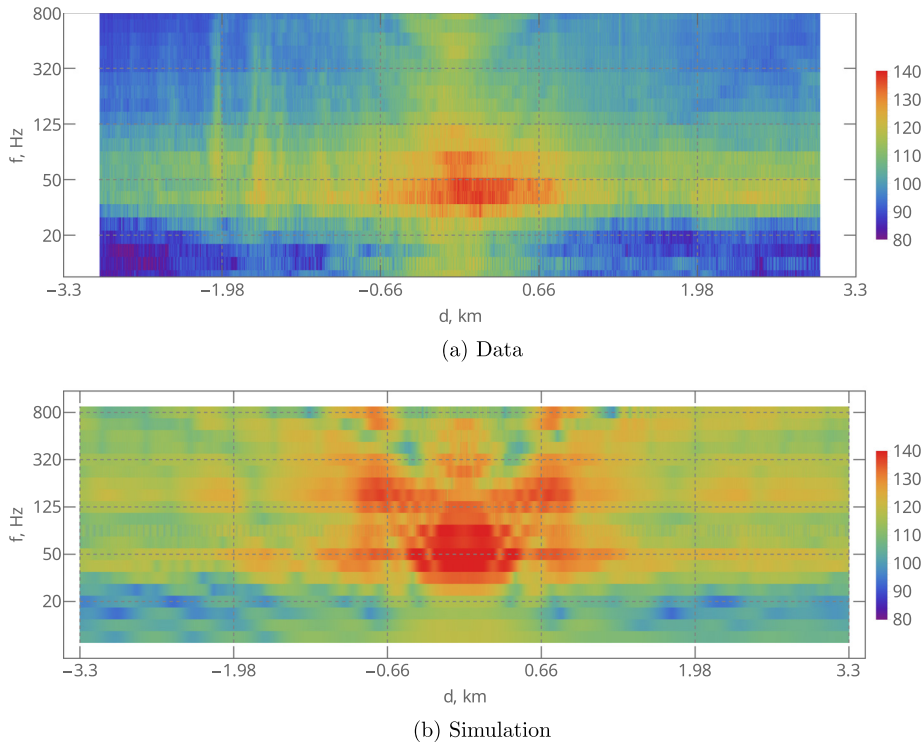


FIG. 6. (Color online) Noise levels (in dB) for the CPA transit obtained from measurement data (a) and the 3D modelling using the parameters provided by the workshop organizers (b).

between the actual hydrological conditions on the measurement day with the historical SSP data, and an inadequate representation of large source as an infinitesimal monopole (i.e., the far-field approximation). While little can be done to properly correct the source directivity pattern both in the vertical and the horizontal plane without undertaking additional measurements, media parameters can be adjusted using the existing data.

Note that the higher intensity of the simulated vessel noise as compared to the data can be (at least partly)

explained by somewhat stronger acoustic contrast across the water-bottom interface and somewhat smaller attenuation in the sediment layer than in the actual environment.

Some features of the field can be analyzed by considering its vertical cross section (e.g., in x, z -plane) shown in Fig. 7(a) for the frequency of 400 Hz (just as an example). A typical feature of the interference pattern is that near the ocean surface, the intensity maximum is located a few hundred meters away in a range from the source (obviously, exactly the same situation could be also observed in

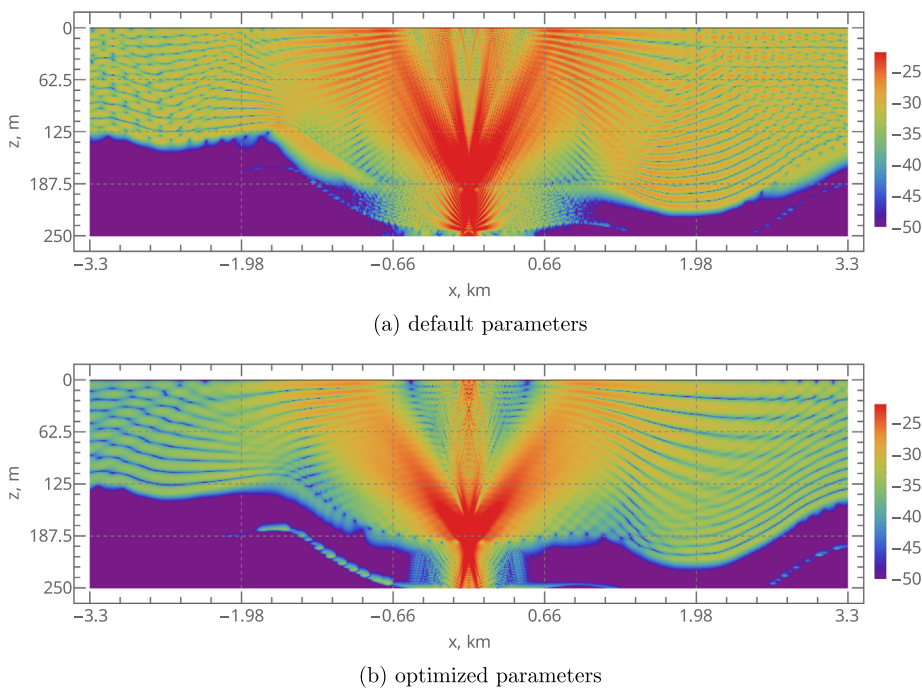


FIG. 7. (Color online) Vertical cross section of acoustic field for $f = 400$ Hz (in dB re 1 m from the source) for the parameters from the scenario description (a) and for the optimized parameter values (b).

non-reciprocal computations). Such interference structure of the field results in the formation of sidelobes in the noise distribution in Fig. 6(b), i.e., elongated features corresponding to high noise intensity areas aligned at an angle of roughly $\pi/4$ to the distance axis. Although similar features can be also found in Fig. 6(a) after a careful examination (and in fact they are natural for the considered source and receiver depths), the respective noise intensity is significantly lower in the measurement data.

Arguably, this discrepancy can partly result from a non-trivial source directivity pattern, while, on the other hand, it can be somewhat mitigated by correcting media parameters (especially for lower frequencies that carry the majority of the source energy).

A. Optimization of media parameters

Since the agreement between the measurements data and the modelling results obtained using the suggested values of geoacoustic parameters was between 10 and 20 dB for almost all decade bands (even at CPA), we decided to perform the optimization of the latter using the CPA levels (for the entire frequency band EC2) as a reference.

The optimization was focused on adjusting bottom parameters, namely, thickness, sound speed, density, and attenuation of the sediment, as well as the sound speed of the substrate. Since differentiating through mode computation is impractical, non-gradient methods were considered. We used the Bayesian optimization method (Garnett, 2023), which quickly explores the target function and finds a value close to the local maximum using only a small number of target function evaluations. The latter is especially important since mode computation takes a considerable amount of time. The Bayesian optimization algorithm can be summarized in the following way

- (1) Given a target function $f : \Theta \mapsto \mathbb{R}$ obtain a prior $p(f|\theta \in \Theta)$, describing how the function is expected to behave with respect to θ . Here Θ is the set of all possible combinations of the optimization parameters (i.e., all possible combinations of bottom parameters).
- (2) Observe $n \in \mathbb{N}$ target function values $y_i = f(\theta_i)$ at randomly selected points $\{\theta_i\}_{i=1}^n$.
- (3) Obtain a posterior $p(f|\theta_1, \dots, \theta_n, y_1, \dots, y_n)$.
- (4) For each $j = \overline{1, m}, m \in \mathbb{N}$ do

- (a) Obtain the next best guess θ_{n+j} by maximizing some acquisition function $q : \Theta \mapsto \mathbb{R}$ that assigns a score to potential guesses based on their perceived ability to benefit the optimization process at the current posterior $p(f|\theta_1, \dots, \theta_{n+j-1}, y_1, \dots, y_{n+j-1})$.
 - (b) Observe the target function value at the newly obtained point $y_{n+j} = f(\theta_{n+j})$.
 - (c) Update the posterior $p(f|\theta_1, \dots, \theta_{n+j}, y_1, \dots, y_{n+j})$.
- (5) Output the maximal value y_i with its respective point θ_i .

The most commonly used prior is that of a Gaussian process (Garnett, 2023). It takes the following form:

$$\begin{bmatrix} f(\theta) \\ f(\theta_1) \\ \vdots \\ f(\theta_n) \end{bmatrix} \sim \mathcal{N} \left(\mu, \begin{bmatrix} k(\theta, \theta) & k(\theta, \theta_1) & \dots & k(\theta, \theta_n) \\ k(\theta_1, \theta) & k(\theta_1, \theta_1) & \dots & k(\theta_1, \theta_n) \\ \vdots & \vdots & \ddots & \vdots \\ k(\theta_n, \theta) & k(\theta_n, \theta_1) & \dots & k(\theta_n, \theta_n) \end{bmatrix} \right), \tag{7}$$

which is a multivariate normal distribution with the mean μ and covariance matrix $\{k(\theta_i, \theta_j)\}_{i,j}$, where $k : \Theta \times \Theta \mapsto \mathbb{R}$ is a so-called kernel or covariance function. The posterior distribution is then given by

$$\begin{aligned} p(f(\theta)|\theta_1, \dots, \theta_n, f(\theta_1), \dots, f(\theta_n)) &\sim \mathcal{N}(m, s^2), \\ m &= \{k(\theta, \theta_i)\}_{i=1}^n \cdot \left(\{k(\theta_i, \theta_j)\}_{i,j=1}^n \right)^{-1} \cdot \{f(\theta_i)\}_{i=1}^n, \\ s^2 &= k(\theta, \theta) - \{k(\theta, \theta_i)\}_{i=1}^n \cdot \left(\{k(\theta_i, \theta_j)\}_{i,j=1}^n \right)^{-1} \\ &\quad \cdot \{k(\theta, \theta_i)\}_{i=1}^n. \end{aligned} \tag{8}$$

For this particular task in our study, we used Matérn kernel,

$$k(\theta_i, \theta_j) = \frac{1}{\Gamma(\nu)^{\nu-1}} \left(\frac{\sqrt{2\nu}}{l} d(\theta_i, \theta_j) \right)^\nu K_\nu \left(\frac{\sqrt{2\nu}}{l} d(\theta_i, \theta_j) \right), \tag{9}$$

where $\nu, l \in \mathbb{R}$ are the kernel parameters, $d(\cdot, \cdot)$ is the Euclidean distance, $K_\nu(\cdot)$ is a modified Bessel function of the second kind, and $\Gamma(\cdot)$ is the gamma function. The parameter ν controls the smoothness of the resulting function (see Fig. 8) and l is the length scale parameter.

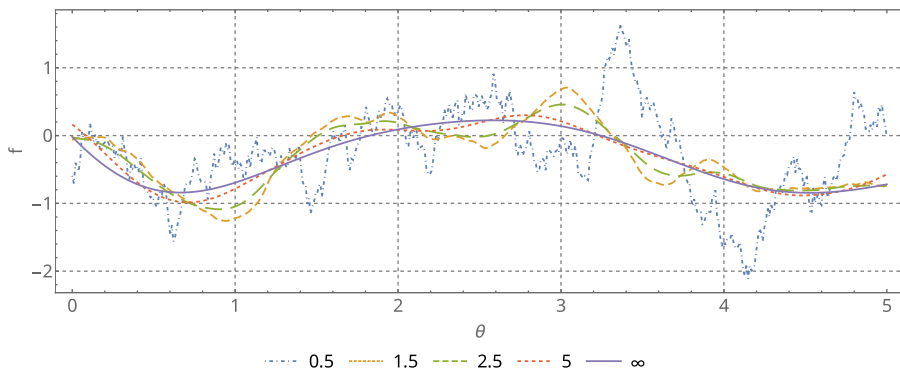


FIG. 8. (Color online) The function $f(\theta)$ sampled from a multivariate normal distribution (7) with zero mean and covariance matrix defined by the Matérn kernel with different values for the parameter ν . $f(\theta)$ and θ are dimensionless and are plotted to show the impact of ν .

The value $\nu = 5/2$ was used and the kernel is transformed to

$$k(\theta_i, \theta_j) = \left(1 + \frac{\sqrt{5}}{l}d(\theta_i, \theta_j) + \frac{5}{3l}d(\theta_i, \theta_j)^2\right) \times \exp\left(-\frac{\sqrt{5}}{l}d(\theta_i, \theta_j)\right). \tag{10}$$

This value provides a good balance between function smoothness and its ability to approximate coarse data and allows for computing the kernel without evaluating the modified Bessel function. The parameter l is initially set to 1 and gets updated during the optimization process to better fit the observed data.

For the acquisition function, Upper Confidence Bound was used,

$$q(\theta) = E[X_\theta] + \kappa\sqrt{\text{Var}(X_\theta)}, \tag{11}$$

where $X_\theta \sim \mathcal{N}(m, s^2)$ is a random variable distributed according to the posterior distribution in Eq. (8). The parameter $\kappa \in \mathbb{R}$ controls the balance of exploitation and exploration with lower values promoting points around the target function peaks and higher values allow points to be selected from the whole range (see Fig. 9).

The optimization was performed in Python using BayesianOptimization library (Nogueira, 2014). To facilitate the process, the mode computation was re-implemented using Tensorflow library (Abadi et al., 2015), which allows the computations to be performed on a GPU and decreases the time it takes to obtain CPA levels for the entire frequency range from several hours to several minutes.

For the target function, the negative mean squared difference between logarithms of the noise level at CPA obtained from measurements data and the modeling results was used,

$$f(\theta) = -\frac{1}{N_F} \sum_{f_c} \left(\log(E_{p,ddec}(f_c, d_{CPA})) - \log(E_{p,ddec}^{mod}(f_c, d_{CPA}, \theta)) \right)^2, \tag{12}$$

where N_F is the number of decade bands taken into account, $E_{p,ddec}^{mod}(f_c, d_{CPA}, \theta)$ is the modeling result for a given central frequency f_c , distance d_{CPA} , and media parameters θ .

The SSP in the water column was also adjusted in the course of the optimization. It was parameterized by a scalar real parameter $t \in [-1, 1]$ (that can be considered time). The profile for a given t was obtained using depth-by-depth interpolation between the three nodes $-1, 0, 1$ as follows:

$$c_{water}(z, t) = \begin{cases} c_{oct}(z) + (t+1)(c_{nov}(z) - c_{oct}(z)), & -1 \leq t \leq 0, \\ c_{nov}(z) + t(c_{dec}(z) - c_{nov}(z)), & 0 < t \leq 1, \end{cases} \tag{13}$$

where $c_{oct}, c_{nov}, c_{dec}$ are the SSPs for October, November, and December, respectively (i.e., each node corresponds to one month, see Fig. 3).

The sound speed in the sediment bottom layer is parameterized as follows:

$$c_{sed}(z) = c_0 + \frac{z - z_b}{\Delta z} \Delta c, \tag{14}$$

where z_b is the bottom depth, Δz is the layer thickness, c_0 is the sound speed at its top (i.e., just below the water-bottom interface), and Δc characterizes the sound velocity gradient in the layer.

The optimization parameter ranges and their values obtained during the optimization process are shown in Table II. Note that the best agreement of the sound levels at CPA is achieved for October sound speed data and for somewhat lower sound speed in the upper part of the sediment layer, as suggested by the workshop organizers. Optimization also results in a much higher sediment attenuation parameter than one might normally expect. This can be explained by the fact that the models we used do not take elasticity effects into account. Since the presence of shear waves in the bottom results in additional loss of acoustic energy, an unrealistically large value of attenuation in an equivalent fluid bottom model must compensate for it. Also, note that the best model-data fit is achieved for the maximum sediment density value in the search interval. This can be explained by the low sensitivity to this parameter which is quite common for geoaoustic inversion problems. We decided not to extend this interval any further in order to keep this value reasonable. The quality of the optimization results can be assessed by comparing the sound level plots in Fig. 5.

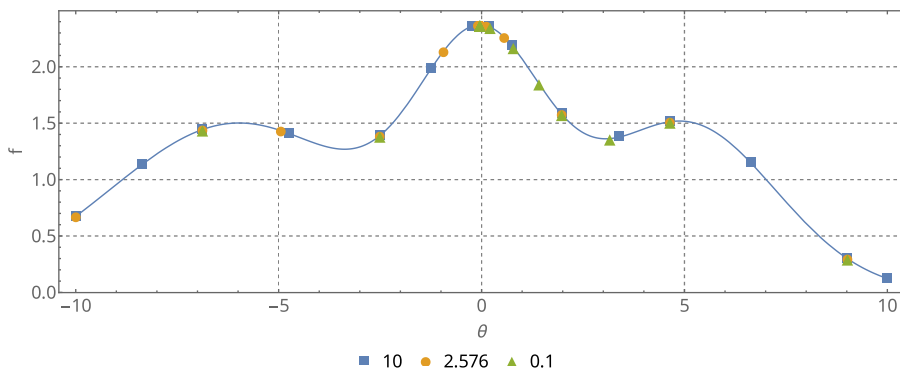


FIG. 9. (Color online) Points selected during Bayesian optimization using Upper Confidence Bound acquisition function with different values for parameter κ . $f(\theta)$ is an arbitrary function the optimization was performed for to show the impact of κ .

TABLE II. Optimization parameters.

	Sediment					Substrate			SSP
	Thickness Δz , m	Sound speed m/s		Density g/cm ³	Attenuation dB/ λ	Sound speed m/s	Density g/cm ³	Attenuation dB/ λ	
		c	Δc						
default	50	1541	50	1.8	0.61	2160	2	0.25	0
optimized	61.4	1519.2	50	2	2.01	1931.5	2	0.25	-1
range	[20, 200]	[1500, 1600]	[0, 100]	[1, 2]	[0.1, 2.5]	[1800, 3000]			[-1, 1]

B. Simulation of the sound levels

After performing optimization of the geoacoustic parameters of the media we simulated the CPA transit sound field again. The results for both the full-3D AMPLE model and its 2D (range-independent) counterpart are shown in Fig. 10. Figure 10 also presents the difference between the two models (it is computed as a difference of fields in the logarithmic units in the first two subfigures). First, one can observe a much better qualitative agreement with the measured sound field shown in Fig. 6. Second, for certain

distances and frequency bands the difference between the 2D and the 3D simulations is about 7–10 dB (it can be even as high as 15 dB for certain points of the noise diagram, however, these points correspond to relatively low sound levels both in the modelling results and in the measurement data). Such a difference can be explained by the influence of the inhomogeneous bottom relief, and, in particular, by the manifestation of the horizontal refraction (Jensen *et al.*, 2011; Katsnelson *et al.*, 2012) of acoustic waves. The significance of this effect can be seen in Fig. 11, where the

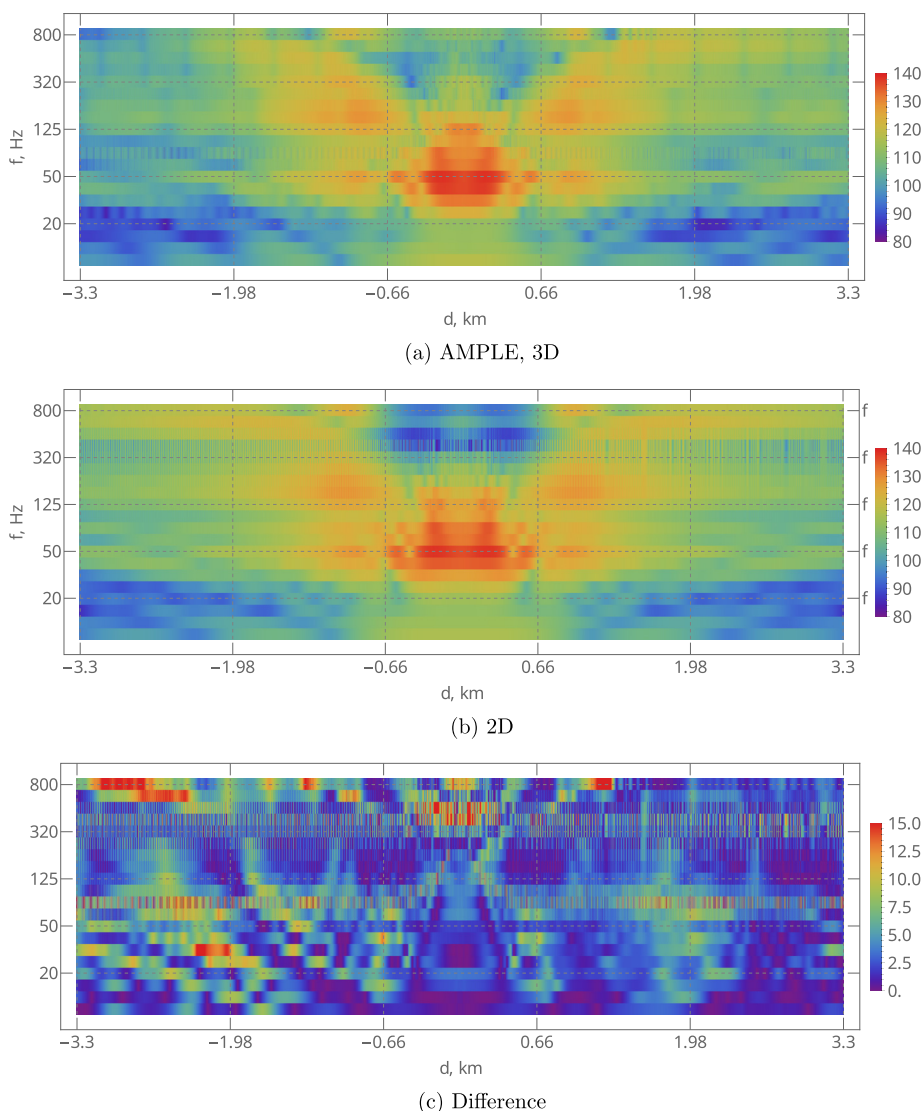


FIG. 10. (Color online) Vessel sound level (in dB) simulated for the CPA transit with the optimized environment parameters.

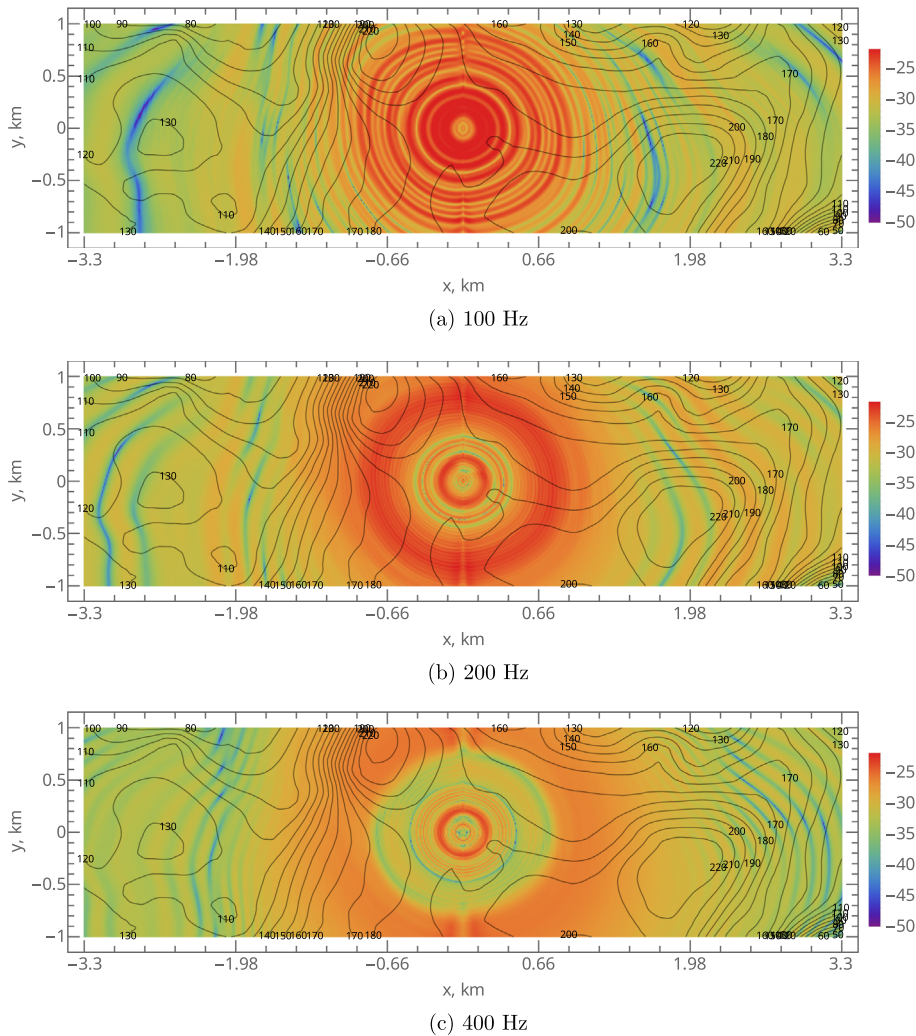


FIG. 11. (color online) Horizontal cross-sections of acoustic field (in dB re 1 m) at individual frequencies obtained as a solution of Eq. (1) (see supplementary material for an animation showing all frequencies). Isobaths in the area are shown by solid black lines.

simulation results for individual frequencies are presented (see also supplementary material to this paper). As expected, the sound is refracted toward the areas with greater water depth, and the wavefronts 1–2 km away from the source no longer resemble circles. Note that the relatively large difference between the predictions obtained using 2D and 3D models near CPA at higher frequencies can be attributed to the fact that it takes smaller propagation distances for the anisotropy of the field in the horizontal plane to develop. As can be seen in Fig. 11, the field at 400 Hz exhibits substantial anisotropy even at distances of about 200 m, while remains relatively isotropic up to ranges $r \sim 1$ km at $f = 100$ and 200 Hz. Clearly, the range at which this effect becomes important is roughly proportional to the wavelength, and therefore at higher frequencies, it becomes noticeable near CPA. It is also important that positioning the source near the bottom creates favorable conditions for the excitation of higher waterborne modes that are more susceptible to horizontal refraction due to inhomogeneous bathymetry. Finally, a juxtaposition of the field and bathymetry isolines in Fig. 11 indicates that the bottom relief effect cannot be accurately simulated within the framework of any 2D

model, as there is strong azimuthal coupling even at close range.

The accuracy of the modelling results obtained for the default and optimized environment parameters is illustrated in Fig. 12, where the difference in the measured noise levels for both waveguide models is presented. It can be seen that the optimization results in a nearly perfect reproduction of the measurement data for all frequencies up to 141 Hz. Note that this frequency range is crucial for environmental impact assessment, as it captures most of the acoustic energy from this source. Major accuracy improvements can be also seen for higher frequencies for the track part near the CPA (namely, for $-0.7 \text{ km} < x < 0.7 \text{ km}$). Certain improvements are also visible for the distant parts, i.e., for $|x| > 2 \text{ km}$. Within these areas of the sound field diagram, the simulation-measurements discrepancy is comparable to the difference between the predictions of 3D and 2D models. Thus, for a substantial part of the sound field, the 3D modelling can actually be important for the estimation accuracy.

V. CONCLUSION AND DISCUSSION

In this study, we performed a numerical simulation of the sound field from a surface vessel moving past a

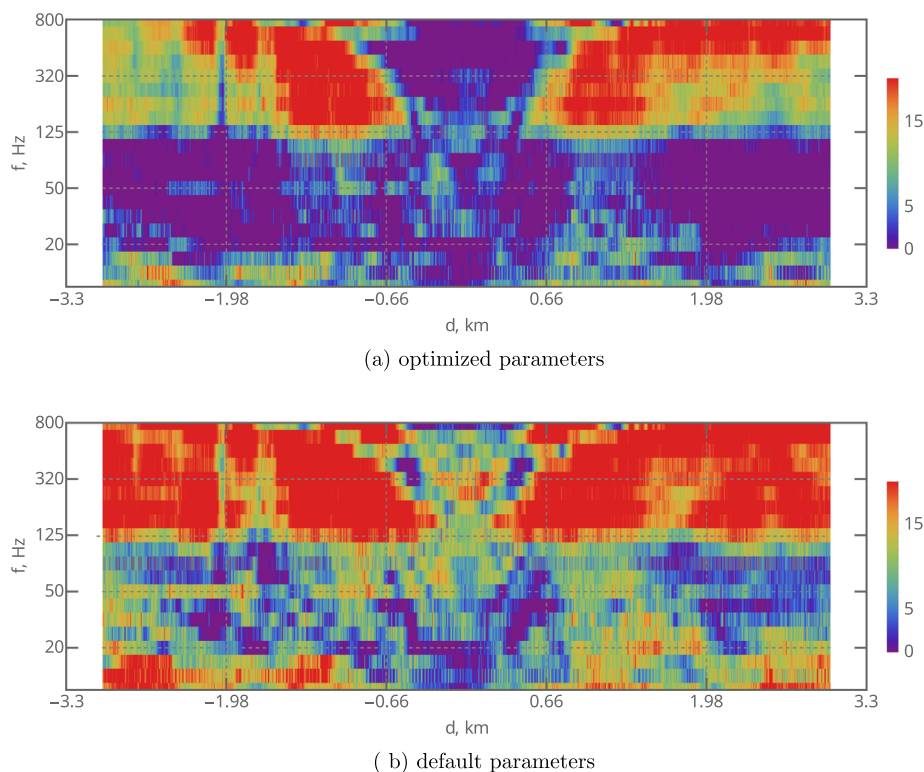


FIG. 12. (Color online) Accuracy of the bulk carrier sound simulation (in dB) for the CPA transit with the optimized media parameters (a) and the parameters suggested in the scenario description (b).

hydrophone system. Such simulations could be of importance to extrapolate estimates of shipping noise emissions to the areas where measurements cannot be accomplished and to assess environmental impacts.

It was shown that accurate simulation of the sound field requires adequate knowledge of the environment parameters. Indeed, the optimization demonstrated that the sound field predictions were particularly sensitive to the acoustic impedance contrast at the seabed. Rough estimates on the basis of geologic maps and tables of typical geoacoustic properties of various rocks and sediments may be insufficient for this purpose. Instead, it is preferable to perform geoacoustic inversion (or, more broadly speaking, fitting of the parameters) using sources of opportunity or by setting up dedicated experiments on the propagation loss measurements. Some approaches to the estimation of the geoacoustic parameters of the bottom are known from the existing literature, e.g., (Gervaise *et al.*, 2012; Knobles, 2015; Tollefsen *et al.*, 2021). In the scenario considered here, the use of the media parameters optimized using the measurements taken at a single point of the vessel track (namely, the CPA) allowed us to substantially improve the accuracy of the sound level prediction.

It is important to stress that the optimized values of media parameters are likely to be somewhat nonphysical and merely parameterize the real bottom in terms of the propagation loss (for instance, an unusually large value of attenuation parameter apparently compensates for the absence of shear waves in the models we used, which can be considered a loss mechanism). Nevertheless, the optimization significantly improved the accuracy of the sound field simulation. It is also worth mentioning that, in our

experience, the use of historical SSP data may not provide an optimal solution. A better option may be to use ocean circulation model predictions, especially for areas where the models assimilate *in situ* measurements.

Our study also highlights the significance of taking into account 3D sound propagation effects when performing the simulation of the sound field. It is important to emphasize however that the use of relatively computationally expensive 3D methods makes sense only after the adjustment of media parameters, as otherwise, much more significant inaccuracy would result from the uncertainty in the values of the latter.

Finally, it is likely that a large vessel cannot actually be accurately represented by a monopole point source, and its directivity pattern both in the horizontal and the vertical plane must be taken into account (Cybulski, 1977; Gassmann *et al.*, 2017), since otherwise, even the CPA-optimized media parameters cannot guarantee perfect reproduction of the sound field over a large frequency range (e.g., EC2). Indeed, the size of the bulk carrier in the considered scenario is comparable to its CPA distance from the hydrophone. Having measurement data that contains the information on the phase (rather than only on the magnitude) variations one can consider a parametrization of the vessel by a set of point sources whose complex spectra can be probably estimated. Representations of vessels as spatially distributed noise sources are a subject of ongoing research at the ULS (Urazghildiiev and Hannay, 2021).

SUPPLEMENTARY MATERIAL

See the supplementary material for an animation showing the horizontal cross-sections of the field (in dB re 1 m)

for all frequencies (note that for the frequencies of 100, 200, and 400 Hz such cross-sections are given in Fig. 11). Note that illusion of movement in the animation is a manifestation of the waveguide invariant (Jensen *et al.*, 2011) properties.

ACKNOWLEDGMENTS

The authors are grateful to Vladimir Nechayuk and Michael Jenkerson (Exxon Mobil) for inviting P.S.P. to participate in the workshop as well as for their useful comments. We are also immensely grateful to Dr. Michael Ainslie and the JASCO team who organized the workshop and provided us all the help and guidance we needed. The work of A.G.T. was supported by the Russian Science Foundation, Project No. 22-11-00171 (<https://rscf.ru/en/project/22-11-00171/>). The work of P.S.P. at POI is within state assignment program No. 121021700341-2.

AUTHOR DECLARATIONS

Conflict of Interest

The authors declare no conflict of interest.

DATA AVAILABILITY

Data availability is not applicable to this article as no new data were collected or analyzed in this study.

Abadi, M., Agarwal, A., Barham, P., Brevdo, E., Chen, Z., Citro, C., Corrado, G. S., Davis, A., Dean, J., Devin, M., Ghemawat, S., Goodfellow, I., Harp, A., Irving, G., Isard, M., Jia, Y., Jozefowicz, R., Kaiser, L., Kudlur, M., Levenberg, J., Mané, D., Monga, R., Moore, S., Murray, D., Olah, C., Schuster, M., Shlens, J., Steiner, B., Sutskever, I., Talwar, K., Tucker, P., Vanhoucke, V., Vasudevan, V., Viégas, F., Vinyals, O., Warden, P., Wattenberg, M., Wicke, M., Yu, Y., and Zheng, X. (2015). "TensorFlow: Large-scale machine learning on heterogeneous systems," available at <https://www.tensorflow.org/> (Last viewed 27 April 2024).

Ainslie, M. A., Halvorsen, M. B., Labak, S., Li, Z., and Lucke, K. (2023). "JIP Acoustic Modelling (JAM Workshop: Workshop Report. Document 02923, Version 2.1)," Technical Report by JASCO Applied Sciences for E&P Sound and Marine Life Joint Industry Programme (JASCO Applied Sciences USA, Silver Spring, MD). (This report will be made available after publication of this J. Acoust. Soc. Am. special issue on Verification and Validation of Source and Propagation Models for Underwater Sound.)

Ainslie, M. A., Halvorsen, M. B., and Robinson, S. P. (2021a). "A terminology standard for underwater acoustics and the benefits of international standardization," *IEEE J. Oceanic Eng.* **47**(1), 179–200.

Ainslie, M., Hannay, D., MacGillivray, A., Trounce, K., and Lucke, K. (2021b). "Proposed alignment of measurement and analysis procedures for quiet ship certifications," Technical report (JASCO Applied Sciences, Victoria, Canada).

Ainslie, M. A., Laws, R. M., and Sertlek, H. Ö. (2019). "International airgun modeling workshop: Validation of source signature and sound propagation models—Dublin (Ireland), July 16, 2016—Problem description," *IEEE J. Oceanic Eng.* **44**(3), 565–574.

Ainslie, M. A., Martin, S. B., Trounce, K. B., Hannay, D. E., Eickmeier, J. M., Deveau, T. J., Lucke, K., MacGillivray, A. O., Nolet, V., and Borys, P. (2022). "International harmonization of procedures for measuring and analyzing of vessel underwater radiated noise," *Mar. Pollut. Bull.* **174**, 113124.

Collins, M. D. (1993). "A split-step Padé solution for the parabolic equation method," *J. Acoust. Soc. Am.* **93**, 1736–1742.

Cybulski, J. (1977). "Probable origin of measured supertanker radiated noise spectra," in *Proceedings of OCEANS'77 Conference Record*, October 17–19, Los Angeles, CA, pp. 184–191.

de Moraes Calazan, R., and Rodríguez, O. C. (2018). "Simplex based three-dimensional eigenray search for underwater predictions," *J. Acoust. Soc. Am.* **143**(4), 2059–2065.

Erbe, C., Marley, S. A., Schoeman, R. P., Smith, J. N., Trigg, L. E., and Embling, C. B. (2019). "The effects of ship noise on marine mammals—A review," *Front. Mar. Sci.* **6**, 606.

Garnett, R. (2023). *Bayesian Optimization* (Cambridge University Press, Cambridge, UK).

Gassmann, M., Wiggins, S. M., and Hildebrand, J. A. (2017). "Deep-water measurements of container ship radiated noise signatures and directionality," *J. Acoust. Soc. Am.* **142**(3), 1563–1574.

Gervaise, C., Kinda, B. G., Bonnel, J., Stéphan, Y., and Vallez, S. (2012). "Passive geoacoustic inversion with a single hydrophone using broadband ship noise," *J. Acoust. Soc. Am.* **131**(3), 1999–2010.

Hannay, D. E., Mouy, X., and Li, Z. (2016). "An automated real-time vessel sound measurement system for calculating monopole source levels using a modified version of ANSI/ASA S12.64-2009," *Can. Acoust.* **44**(3), 3002, available at <https://jcaa.caa-aca.ca/index.php/jcaa/article/view/3002>.

ISO (2017). ISO 18405:2017, "Underwater acoustics—Terminology" (ISO, Geneva, Switzerland).

Jensen, F. B., Kuperman, W. A., Porter, M. B., and Schmidt, H. (2011). *Computational Ocean Acoustics* (Springer Science & Business Media, New York).

Jiang, P., Lin, J., Sun, J., Yi, X., and Shan, Y. (2020). "Source spectrum model for merchant ship radiated noise in the Yellow Sea of China," *Ocean Eng.* **216**, 107607.

Katsnelson, B., Petnikov, V., and Lynch, J. (2012). *Fundamentals of Shallow Water Acoustics* (Springer Science & Business Media, New York).

Knobles, D. P. (2015). "Maximum entropy inference of seabed attenuation parameters using ship radiated broadband noise," *J. Acoust. Soc. Am.* **138**(6), 3563–3575.

Lin, Y.-T., Duda, T. F., and Newhall, A. E. (2013). "Three-dimensional sound propagation models using the parabolic-equation approximation and the split-step Fourier method," *J. Comput. Acoust.* **21**(01), 1250018.

MacGillivray, A., and de Jong, C. (2021). "A reference spectrum model for estimating source levels of marine shipping based on automated identification system data," *J. Mar. Sci. Eng.* **9**(4), 369.

MacGillivray, A. O., Ainsworth, L. M., Zhao, J., Dolman, J. N., Hannay, D. E., Frouin-Mouy, H., Trounce, K. B., and White, D. A. (2022). "A functional regression analysis of vessel source level measurements from the Enhancing Cetacean Habitat and Observation (ECHO) database," *J. Acoust. Soc. Am.* **152**(3), 1547–1563.

Merchant, N. D., Blondel, P., Dakin, D. T., and Dorocicz, J. (2012). "Averaging underwater noise levels for environmental assessment of shipping," *J. Acoust. Soc. Am.* **132**(4), EL343–EL349.

Nogueira, F. (2014). "Bayesian Optimization: Open source constrained global optimization tool for Python," available at <https://github.com/fmfn/BayesianOptimization> (Last viewed 27 April 2024).

Oliveira, T. C., Lin, Y.-T., and Porter, M. B. (2021). "Underwater sound propagation modeling in a complex shallow water environment," *Front. Mar. Sci.* **8**, 751327.

Özkan Sertlek, H., and Ainslie, M. A. (2014). "A depth-dependent formula for shallow water propagation," *J. Acoust. Soc. Am.* **136**(2), 573–582.

Petrov, P., and Tyshchenko, A. (2020). "Ample mode parabolic equation," available at <https://github.com/GoldFeniks/Ample>.

Petrov, P., Zaikin, O., and Tyshchenko, A. (2020). "Cambala: Coupled acoustic modes with bottom attenuation in linear acoustics," available at <https://github.com/Nauchnik/CAMBALA>.

Petrov, P. S., and Antoine, X. (2020). "Pseudodifferential adiabatic mode parabolic equations in curvilinear coordinates and their numerical solution," *J. Comput. Phys.* **410**, 109392.

Petrov, P. S., Ehrhardt, M., and Kozitskiy, S. B. (2024). "A generalization of the split-step Padé method to the case of coupled acoustic modes equation in a 3D waveguide," *J. Sound Vib.* **577**, 118304.

Petrov, P. S., Ehrhardt, M., Tyshchenko, A. G., and Petrov, P. N. (2020). "Wide-angle mode parabolic equations for the modelling of horizontal refraction in underwater acoustics and their numerical solution on unbounded domains," *J. Sound Vib.* **484**, 115526.

- Porter, M. B. (2019). "Beam tracing for two-and three-dimensional problems in ocean acoustics," *J. Acoust. Soc. Am.* **146**(3), 2016–2029.
- Sertlek, H. Ö., Ainslie, M. A., and Heaney, K. D. (2018). "Analytical and numerical propagation loss predictions for gradually range-dependent isospeed waveguides," *IEEE J. Oceanic Eng.* **44**(4), 1240–1252.
- Simard, Y., Roy, N., Gervaise, C., and Giard, S. (2016). "Analysis and modeling of 255 source levels of merchant ships from an acoustic observatory along St. Lawrence Seaway," *J. Acoust. Soc. Am.* **140**(3), 2002–2018.
- Southall, B. L., Finneran, J. J., Reichmuth, C., Nachtigall, P. E., Ketten, D. R., Bowles, A. E., Ellison, W. T., Nowacek, D. P., and Tyack, P. L. (2019). "Marine mammal noise exposure criteria: Updated scientific recommendations for residual hearing effects," *Aquat. Mamm.* **45**(2), 125–232.
- Southall, B. L., Scholik-Schlomer, A. R., Hatch, L., Bergmann, T., Jasny, M., Metcalf, K., Weilgart, L., and Wright, A. J. (2017). *Underwater Noise from Large Commercial Ships – International Collaboration for Noise Reduction* (John Wiley and Sons, Ltd, New York), pp. 1–9.
- Sturm, F. (2016). "Leading-order cross term correction of three-dimensional parabolic equation models," *J. Acoust. Soc. Am.* **139**(1), 263–270.
- Tollefsen, D., Hodgkiss, W. S., Dosso, S. E., Bonnel, J., and Knobles, D. P. (2021). "Probabilistic estimation of merchant ship source levels in an uncertain shallow-water environment," *IEEE J. Oceanic Eng.* **47**(3), 647–656.
- Tyshchenko, A., Zaikin, O., Sorokin, M., and Petrov, P. (2021). "A program based on the wide-angle mode parabolic equations method for computing acoustic fields in shallow water," *Acoust. Phys.* **67**, 512–519.
- Urazghildiiev, I. R., and Hannay, D. E. (2021). "Localization of ship noise feasibility and application study: Using the Boundary Pass Underwater Listening Station compact acoustic arrays," Technical report for the Enhancing Cetacean Habitat and Observation (ECHO) Program JASCO document 02380 (JASCO, Victoria, Canada).
- Wales, S. C., and Heitmeyer, R. M. (2002). "An ensemble source spectra model for merchant ship-radiated noise," *J. Acoust. Soc. Am.* **111**(3), 1211–1231.